Tunnelling and Underground Space Technology 179 (2027) 108146

Contents lists available at ScienceDirect

Tunnelling and Underground Space Technology incorporating Trenchless Technology Research

journal homepage: www.elsevier.com/locate/tust

Influence of tunnel-fault intersection angle on the seismic deformation mode of a large-span cross-fault subsea tunnel

Yang Gao [a,b], Ke Zhang [c], Hao Wang [c], Zerui Ji [c], Chao Luo [c,*]

[a] Yanzhao Modern Transportation Laboratory of Shijiazhuang Tiedao University, Shijiazhuang 050043, China
[b] School of Safety Engineering and Emergency Management, Shijiazhuang Tiedao University, Shijiazhuang 050043, China
[c] School of Civil Engineering, Shijiazhuang Tiedao University, Shijiazhuang 050043, China

ARTICLE INFO

Keywords:
Tunnel engineering
Cross-fault tunnel
Physics-based source model
Tunnel-fault intersection angle
Non-uniform excitation

ABSTRACT

Cross-fault subsea tunnels are subjected to spatially non-uniform seismic motion and fault-induced permanent displacement, but the role of the tunnel-fault intersection angle remains difficult to evaluate when fault rupture is represented only by prescribed offsets. Taking the Qingdao Jiaozhou Bay Second Subsea Tunnel crossing the Cangkou Fault as an engineering case, this study combines deterministic ground-motion simulation with modified domain reduction method (MDRM) seismic input to investigate the seismic response of a large-span cross-fault subsea tunnel. The simulated cross-fault seismic field shows that the surrounding rock at tunnel depth is affected by both fault-parallel and fault-normal displacement components; the latter is smaller but non-negligible. Under the actual intersection angle of 27 degrees, the tunnel displacement varies smoothly along the alignment because the tunnel passes above the fault core, with a cumulative lateral displacement of about 6 cm and a longitudinal compression of about 11 cm. Across the six discrete alignment cases, the peak normal and shear strain components exhibit different, non-monotonic patterns. The hoop and longitudinal normal strains are relatively large and the shear strain is smallest at 42°, whereas the shear component is larger at 12°, 72° and 87°; the maximum equivalent strain occurs at 57°, where both normal and shear components remain appreciable. These results indicate that changing the tunnel alignment within the prescribed earthquake-source and regional-site model, together with the associated change in spatial ground-motion sampling, primarily modifies the normal–shear strain combination rather than monotonically amplifying the overall strain level.

1. Introduction

Tunnels and underground structures are increasingly constructed in seismically active regions as transportation networks expand across mountainous, coastal, and urban areas. Although underground structures are generally less vulnerable to inertia-dominated seismic damage than aboveground structures, earthquake damage records and post-earthquake investigations have shown that underground openings and tunnels may still experience cracking, lining deformation, and local instability under strong seismic shaking (Dowding & Rozen, 1978; Sharma & Judd, 1991). This risk becomes more critical when adverse geological conditions, active faults, or spatially non-uniform ground deformation are involved. Previous studies have shown that the seismic response of underground structures is strongly affected by ground motion characteristics, surrounding ground deformation, and soil-structure or rock-structure interaction (Hashash et al., 2001; Tsinidis et al., 2020). For tunnels crossing active faults, the seismic demand is more complex because the structure is subjected not only to transient seismic waves but also to permanent fault-induced ground displacement, and recent shaking-table evidence has further highlighted the importance of fault-side relative motion in characterizing lining strain demand (Luo et al., 2026). Therefore, a reliable seismic response analysis method is required for cross-fault tunnels, especially for long subsea tunnels where the geological environment, burial depth, and alignment constraints are more complicated (Xia et al., 2024).

Existing studies on tunnels and buried structures crossing active faults have commonly simplified fault rupture effects as quasi-static ground deformation. In such analyses, a prescribed fault offset is imposed on a local tunnel-ground or soil-structure model, and the structural response is evaluated under simplified normal, reverse, or strike-slip faulting conditions (Anastasopoulos et al., 2008; Karamitros et al., 2011). This approach is effective for identifying the influence of

* Corresponding author.
E-mail address: luochao@stdu.edu.cn (C. Luo).

https://doi.org/10.1016/j.tust.2026.108146
Received 8 June 2026; Received in revised form 10 September 2026; Accepted 21 September 2026

fault type, fault displacement, fault dip, burial depth, and tunnel-fault intersection angle on structural deformation, internal forces, and potential damage zones (Qiao et al., 2022; Vazouras et al., 2012). For tunnel structures, analytical and numerical studies based on imposed fault displacement have shown that longitudinal deformation, bending moment, shear force, and lining strain tend to concentrate near the fault zone or near the interface between different moving ground blocks (Qiao et al., 2022; Zhao et al., 2023). However, the quasi-static treatment has inherent limitations for seismic response analysis of cross-fault tunnels. First, the imposed fault offset is usually determined from empirical magnitude-displacement relationships or assumed displacement patterns, rather than from the physical rupture process of the seismogenic fault. Second, this method neglects the transient seismic waves radiated during fault rupture and therefore cannot represent the spatially non-uniform dynamic ground motion field around the tunnel. Third, when fault displacement and seismic waves are introduced separately, the relative contribution and interaction between permanent ground displacement and transient wave motion remain difficult to quantify. Therefore, a more physically consistent seismic input method is required to capture the coupled effects of fault rupture, fault-induced permanent displacement, and seismic wave propagation on cross-fault tunnel response.

To overcome the limitations of quasi-static fault-displacement methods, dynamic seismic input techniques developed for site response and soil-structure interaction problems have been introduced into underground-structure analysis. The finite dynamic modelling of infinite media provides an important theoretical basis for localized dynamic analysis with artificial boundaries (Lysmer & Kuhlemeyer, 1969). The domain reduction method (DRM) further provides a rigorous framework for applying equivalent seismic forces to a reduced computational domain using free-field motion histories obtained from a larger-scale wave propagation model (Bielak et al., 2003; Yoshimura et al., 2003). The modified domain reduction method (MDRM) improves the accuracy of equivalent seismic input by correcting the errors generated in the original DRM formulation, and it can be combined with viscoelastic artificial boundaries to absorb outgoing scattered waves and reduce boundary-induced errors in tunnel-surrounding rock finite element models (Luo et al., 2019; H. Wang et al., 2021). Meanwhile, physics-based ground motion simulation methods make it possible to generate spatially variable near-fault ground motions that account for source rupture, path effects, and site conditions. The Graves-Pitarka broadband simulation method and the SCEC Broadband Platform have been widely used for generating realistic strong ground motions under kinematic rupture scenarios (Graves & Pitarka, 2015, 2016; Maechling et al., 2015). By combining deterministic ground motion simulation with MDRM-based seismic input and viscoelastic artificial boundaries, the coupled effects of fault-induced permanent displacement and seismic wave propagation can be represented in a more physically consistent manner.

Despite these advances, how the seismic response of a cross-fault tunnel differs among tunnel–fault alignment configurations remains insufficiently resolved. The intersection angle changes how fault-induced ground deformation is projected onto the longitudinal and transverse directions of the tunnel, and therefore affects the axial, bending, and shear deformation of the lining. Existing studies have mainly examined this problem using prescribed fault offsets and have reported displacement, stress, strain, or damage indices for selected crossing angles (Luo et al., 2023; Qiao et al., 2022). However, it is still unclear whether a change in intersection angle simply increases or decreases the overall response level, or instead changes the relative contributions of compression and shear deformation. This distinction is important for alignment selection and seismic mitigation, because a smaller value of one strain component does not necessarily correspond to a less unfavorable combined deformation state (Zhu et al., 2023).

The Qingdao Jiaozhou Bay Second Subsea Tunnel provides a representative engineering case for addressing this question. The tunnel crosses the Cangkou Fault, which is dominated by strike-slip motion with a reverse component, and the tunnel alignment passes above the fault rather than directly through the fault core. In this study, a physics-based seismic source approach is used to generate the cross-fault ground-motion field at the project site, and the resulting motions are introduced into a local tunnel-surrounding rock finite element model through MDRM-based equivalent seismic loads. The analysis first clarifies the response of the actual alignment and then compares six tunnel–fault alignment configurations to characterize their displacement responses, strain distributions and normal–shear strain combinations.

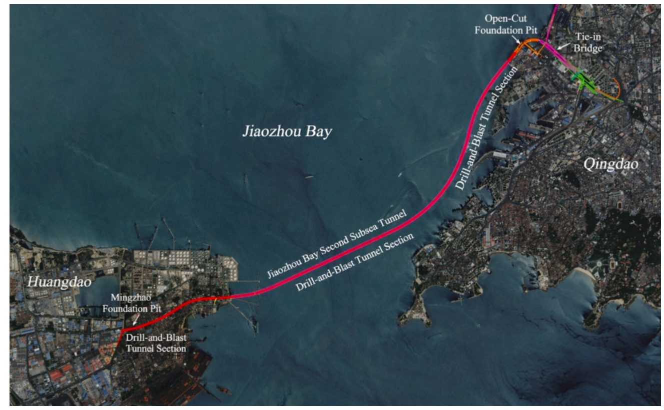

Fig. 1. Location and alignment of the Qingdao Jiaozhou Bay Second Subsea Tunnel.

The contribution of this study lies in applying physics-based regional ground-motion simulation and MDRM input to investigate the alignment-dependent response of a real large-span subsea tunnel within a fixed rupture-generated regional ground-motion field. First, the six tunnel alignments are rotated about a common reference point while the prescribed earthquake-source and regional-site model is kept unchanged, allowing the influence of alignment orientation and the associated spatial ground-motion sampling to be examined. Second, the study identifies the response characteristics of a tunnel that passes above rather than directly through the fault core, including smooth longitudinal displacement together with spatially non-uniform strain and local lining yielding. Third, the results reveal distinct, non-monotonic normal–shear strain combinations among the six alignment configurations, providing a more specific response descriptor than peak equivalent strain alone.

2. Project overview

The Qingdao Jiaozhou Bay Second Subsea Tunnel connects the urban area of Qingdao with Huangdao District and forms a key component of the high-capacity expressway network in Qingdao. Its alignment layout is shown in Fig. 1. The project has a main alignment length of 17.5 km, including 14.37 km of tunnel sections, with the subsea and onshore tunnel sections measuring 9.95 km and 4.41 km, respectively. The tunnel is constructed using a combination of the drill-and-blast method and shield tunnelling, with open-cut foundation pits and tie-in works arranged at both ends. The project adopts a bidirectional six-lane main tunnel system with a central service tunnel. The main tunnel has a cross-sectional width of 15 m, and the lining is constructed using C60 high-performance concrete.

According to the geotechnical investigation report (China Railway Major Bridge Survey and Design Institute Group Co., Ltd., 2022), the overall surrounding rock grade of the subsea section of the Qingdao Jiaozhou Bay Second Subsea Tunnel is Grade III. The shear wave velocity of the surrounding rock was determined based on the unified lithospheric velocity model for continental China, USTClitho2.0 (Han et al., 2022). The mechanical parameters of the tunnel lining and

Table 1
Mechanical parameters of the tunnel lining and surrounding rock used in the numerical model.

Material type	Elastic modulus (GPa)	Density (kg/m^3)	Poisson's ratio	Shear wave velocity (m/s)	Damping ratio
Tunnel lining	36	2400	0.2	2500	0.05
Surrounding rock	44.5	2122	0.22	3578	0.003

surrounding rock used in the numerical model are listed in Table 1.

3. Physics-based seismic response analysis method for cross-fault tunnels

3.1. Physics-based seismic response analysis framework

Cross-fault tunnels are affected by both fault displacement and seismic wave propagation during earthquakes. This study adopts the physics-based seismic source approach proposed by Luo et al. (2024b) to analyze the seismic response of the Qingdao Jiaozhou Bay Second Subsea Tunnel under the combined action of fault-induced permanent displacement and transient ground motion. A large-scale deterministic ground-motion simulation is first conducted to generate the cross-fault seismic field at the engineering site. The simulated motions are then transformed into equivalent seismic loads on the boundaries of the local tunnel-surrounding rock finite element model using MDRM. In this way, fault rupture, seismic-wave propagation, and tunnel structural response are represented within a consistent physical framework. The procedure consists of the following three steps:

Step 1: Deterministic ground motion simulation

The size and origin of the simulation domain are first determined. Based on a kinematic fault rupture model, cross-fault ground motions are simulated using the finite difference method. The resulting seismic motion histories at the corresponding positions of the finite element model boundaries on both sides of the fault are then extracted.

Step 2: Calculation of equivalent seismic loads

A tunnel-surrounding rock finite element model crossing the fault is established. The cross-fault ground motion field obtained in Step 1 is converted into equivalent seismic loads acting on the boundary nodes of the finite element model using MDRM. The equivalent load vector is expressed as Eq. (1).

$$P_{eff}^{MDRM} = \begin{Bmatrix} 0 \\ -M_{be}^{\Omega^+}\ddot{u}_e^0 - C_{be}^{\Omega^+}\dot{u}_e^0 - K_{be}^{\Omega^+}u_e^0 \\ M_{eb}^{\Omega^+}\ddot{u}_b^0 + C_{eb}^{\Omega^+}\dot{u}_b^0 + K_{eb}^{\Omega^+}u_b^0 \end{Bmatrix} \tag{1}$$

where M, C, and K are the mass, damping, and stiffness matrices of the finite element model, respectively. Ω is the local site domain containing the finite element model, and Ω^+ is the complementary domain containing the fault and seismic source. The interface between these two domains is denoted by Γ. The subscripts b and e indicate the nodes on the truncated boundary Γ and in the exterior domain, respectively. u^0 , $\dot{u}^0$, and $\ddot{u}^0$ are the free-field displacement, velocity, and acceleration, respectively. Thus, the equivalent cross-fault seismic loads can be calculated solely from the free-field motion histories at the boundary nodes.

Step 3: Seismic response analysis of the tunnel structure

The equivalent seismic loads obtained in Step 2 are applied to the boundaries of the tunnel-surrounding rock finite element model, and the seismic response of the cross-fault tunnel is then calculated. In this framework, the earthquake source was represented by the finite-fault geometry and the prescribed space–time evolution of slip. The regional simulation generated the associated spatially variable free-field motions, including transient and permanent displacement components, which were introduced into the local tunnel–rock model through MDRM equivalent boundary loads. The local model did not contain a discrete fault surface, fault-interface element, or contact formulation.

The reliability of the local dynamic model was controlled through the consistency of the seismic-input and structural-response models. The boundary motions applied by MDRM were extracted from the same deterministic ground-motion simulation used to characterize the cross-fault seismic field, so the permanent and transient components of motion were not introduced as independent assumptions. The model size, mesh size, and artificial boundary configuration were selected according to the wave-propagation and MDRM criteria described below. These controls are intended to make the subsequent comparison among intersection-angle cases internally consistent, although the results remain specific to the adopted fault source, burial depth, and tunnel configuration.

3.2. Finite element model of the tunnel-surrounding rock system

The Cangkou Fault crossed by the Qingdao Jiaozhou Bay Second Subsea Tunnel is a strike-slip fault, and the seismic motion at the project site is primarily horizontal. The influence of seawater on the seismic motion at tunnel depth is considered negligible and is therefore not explicitly included in the numerical model (Zhang, 2012). A three-dimensional finite element model of the tunnel-surrounding rock system incorporating the seabed topography was established, with artificial boundaries applied to represent the infinite domain outside the computational region. According to Luo et al. (2019), when the ratio of the finite element model width (d_v) to the core-zone width (d_b) exceeds 2, the use of the modified domain reduction method (MDRM) together with viscoelastic artificial boundaries can limit the relative error in peak ground acceleration (PGA) to within 5%. In this study, the core zone of the tunnel cross-section was defined as 80 m in both length and width, and the cross-sectional width of the tunnel-surrounding rock finite element model was conservatively set to 480 m, resulting in $d_v/d_b = 6$. The model height was scaled proportionally, with the distance from the model base to the seabed reaching up to 280 m. To fully capture the seismic response of the tunnel under cross-fault ground motion and to observe the spatial influence of the cross-fault motion on the structure, the longitudinal length of the finite element tunnel model was set to 5.4 km.

According to the mesh-size criterion proposed by Kuhlemeyer and Lysmer (1973), the finite element size used for wave propagation analysis should not exceed one-eighth of the minimum wavelength. For seismic waves within the frequency range of 0–10 Hz, the allowable element size, Δh, can be estimated using Eq. (2).

$$\Delta h \leqslant \frac{\lambda_{\min}}{8} = \frac{3578/10}{8} = 44.725\, m \tag{2}$$

Since the tunnel model is mainly located in the shield tunnelling section, a circular single-bore tunnel lining model was established. The lining thickness is 0.65 m, and the inner and outer diameters are 13.7 m and 15 m, respectively. The surrounding rock was represented by a linear-elastic constitutive model, with zoned material properties determined from the velocity structure adopted in the regional ground-motion simulation. The tunnel lining was represented using a pressure-dependent elastoplastic concrete model. The uniaxial compressive strength, tensile strength, and biaxial compressive strength

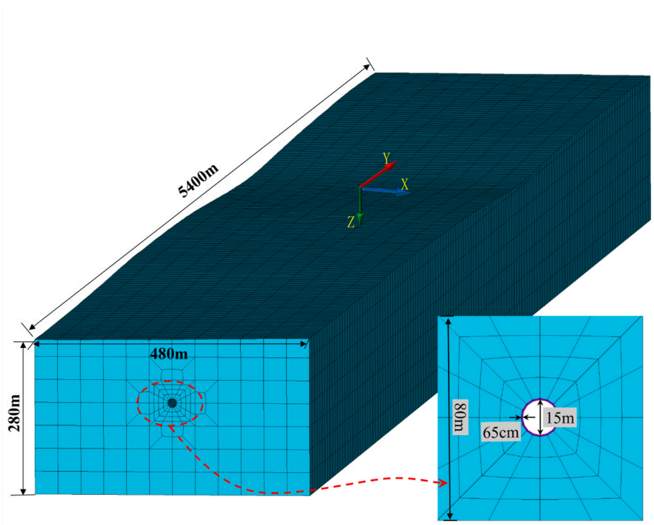

Fig. 2. Finite element model of the tunnel-surrounding rock system.

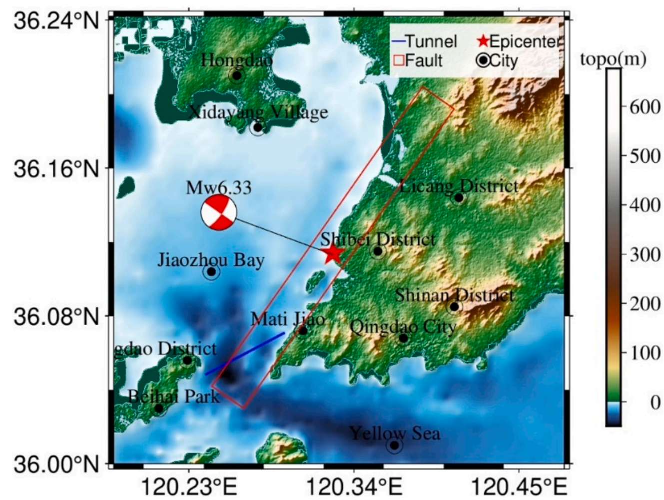

Fig. 3. Ground motion simulation domain showing topography, seabed bathymetry, fault projection, epicenter, and tunnel alignment.

specified for the concrete model were 27.5, 2.04, and 33.0 MPa, respectively. These strength parameters define the compressive and tensile Drucker–Prager yield surfaces. The plastic potential follows an associated flow rule, and the post-yield response is represented as perfectly plastic. Tensile yielding is governed by the Drucker–Prager tension surface calibrated using the uniaxial tensile strength. The lining and surrounding rock were connected through shared nodes to maintain displacement continuity. The mechanical parameters used for the tunnel lining and surrounding rock are listed in Table 1. The established finite element model is shown in Fig. 2, containing 23,760 elements and 25,432 nodes. The origin of the global Cartesian coordinate system is located at sea level; the y-axis is aligned with the tunnel longitudinal direction, the x-axis corresponds to the transverse direction of the model, and the positive z-axis points vertically downward.

The numerical framework was verified by comparing the recovered displacement responses of a tunnel-free MDRM local model for the 27° case with the collocated reference free-field motions obtained from the regional SW4 simulation. In accordance with the validation principle of the domain-reduction method, the reduced local model was required to recover the prescribed background motion after removal of the local structure. At 264 collocated centerline stations at depths of 80 and 200 m, the median displacement correlations were 0.999898 and 0.999907, and the median NRMSEs were 1.72% and 2.47%, respectively. At stations adjacent to the model ends, the corresponding median correlations remained above 0.9997 and the median peak-displacement errors were below 2.4%. After removal of the final offsets, the median late-time discrepancies during 20–30 s were below 0.007% of the reference peak and did not increase relative to the interior stations, indicating that no discernible boundary-reflected contribution entered the region of interest.

Mesh resolution was evaluated using a controlled shear-wave propagation benchmark against the analytical travelling-wave solution. Time-step adequacy was assessed using the same benchmark together with direct time-step refinement of the complete tunnel-free model. Refinement from 40 to 20 and 10 m produced an overall decrease in peak-amplitude, phase and Fourier-amplitude differences. For the adopted 40 m mesh, the peak and Fourier-amplitude differences remained below 1% over 0–10 Hz. The adopted time step, its half and its quarter were assessed using the same measures; a direct half-step analysis of the complete model produced median displacement NRMSEs below 0.004%, maximum peak differences below 0.014% and median Fourier-amplitude differences below 0.15%. These results demonstrate that the adopted mesh and time step are sufficient for the reported displacement response.

3.3. Cross-fault ground motion simulation

To obtain the cross-fault ground motion field for the region containing the tunnel-surrounding rock finite element model, cross-fault ground motion simulation was performed for the Jiaozhou Bay area using SW4, a fourth-order finite-difference code developed by Lawrence Livermore National Laboratory (Petersson & Sjögreen, 2017). The simulation domain is shown in Fig. 3, where the red rectangle denotes the surface projection of the fault plane and the yellow line indicates the location of the tunnel-surrounding rock finite element model. The origin of the simulation domain was set at 35.057°N and 120.264°E, and the domain size was 26 km × 26 km in the north–south and east–west directions. The topographic data for the Jiaozhou Bay area were obtained from 30-m-resolution SRTM1 data released by the U.S. Geological Survey (Farr et al., 2007), and the subsurface velocity structure was constructed using USTClitho2.0 and CRUST1.0 (Laske et al., 2013). The attenuation of P and S waves during propagation was described using quality factors, which were calculated according to the empirical relationships proposed by Graves and Pitarka (2016).

$$Q_S = V_S \times 50 \tag{3}$$

$$Q_P = 2 \times Q_S \tag{4}$$

where Q_P is the P-wave quality factor, Q_S is the S-wave quality factor, and V_S denotes the shear wave velocity, expressed in km/s.

Consistent with the grid-size criterion used for the tunnel-surrounding rock finite element model, the grid spacing of the ground motion simulation domain should not exceed one-eighth of the minimum wavelength when simulating seismic waves within the frequency range of 0–10 Hz. Therefore, a conservative grid spacing of 40 m was adopted for the ground motion simulation. According to fault-related studies in the Jiaozhou Bay area (Luan et al., 2010; Luan & Zhang, 2001) and the seismic safety evaluation report of the project site (J. Wang, 2021), the Danshan-Jiaozhou segment of the Cangkou Fault crossed by the tunnel is a right-lateral strike-slip fault with a reverse component. The fault strike ranges from 35° to 45°, the dip angle ranges from 60° to 80°, and the rupture length is approximately 22 km. Based on the empirical relationships among rupture length, rupture width, and moment magnitude for strike-slip faults proposed by Wells and Coppersmith (1994), the maximum potential earthquake magnitude of the fault was estimated as follows:

$$\log(RLD) = -2.57 + 0.62 \times M_W \tag{5}$$

Table 2
Source parameters used in the GP fault rupture model.

Parameter	Value	Parameter	Value
Strike	35°	Epicentral longitude	120.326°
Dip angle	75°	Epicentral latitude	36.117°
Rake angle	180°	Hypocentral depth	6.5 km
Rupture length	22 km	Moment magnitude	6.33
Rupture width	9 km	Number of subfaults	123,750
Fault top depth	2 km	Subfault size	0.04 km × 0.04 km

$$\log(R_W) = -0.76 + 0.27 \times M_W \quad (6)$$

where RLD is the rupture length, R_W is the rupture width, and M_W is the moment magnitude. Based on these relationships, the rupture width of the Danshan-Jiaozhou Bay segment of the Cangkou Fault was estimated to be approximately 9 km, and its maximum potential earthquake magnitude was determined as M_W 6.33.

The fault rupture model was generated using the Graves-Pitarka (GP) method (Graves & Pitarka, 2015). This method has been applied and validated in strong ground motion simulations of several historical

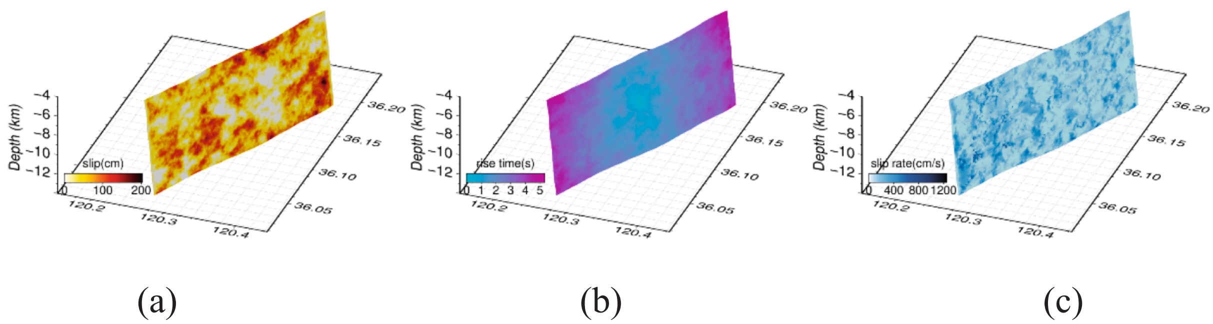

Fig. 4. Fault rupture model showing distributions of (a) slip, (b) rupture initiation time, and (c) peak slip rate on the fault plane.

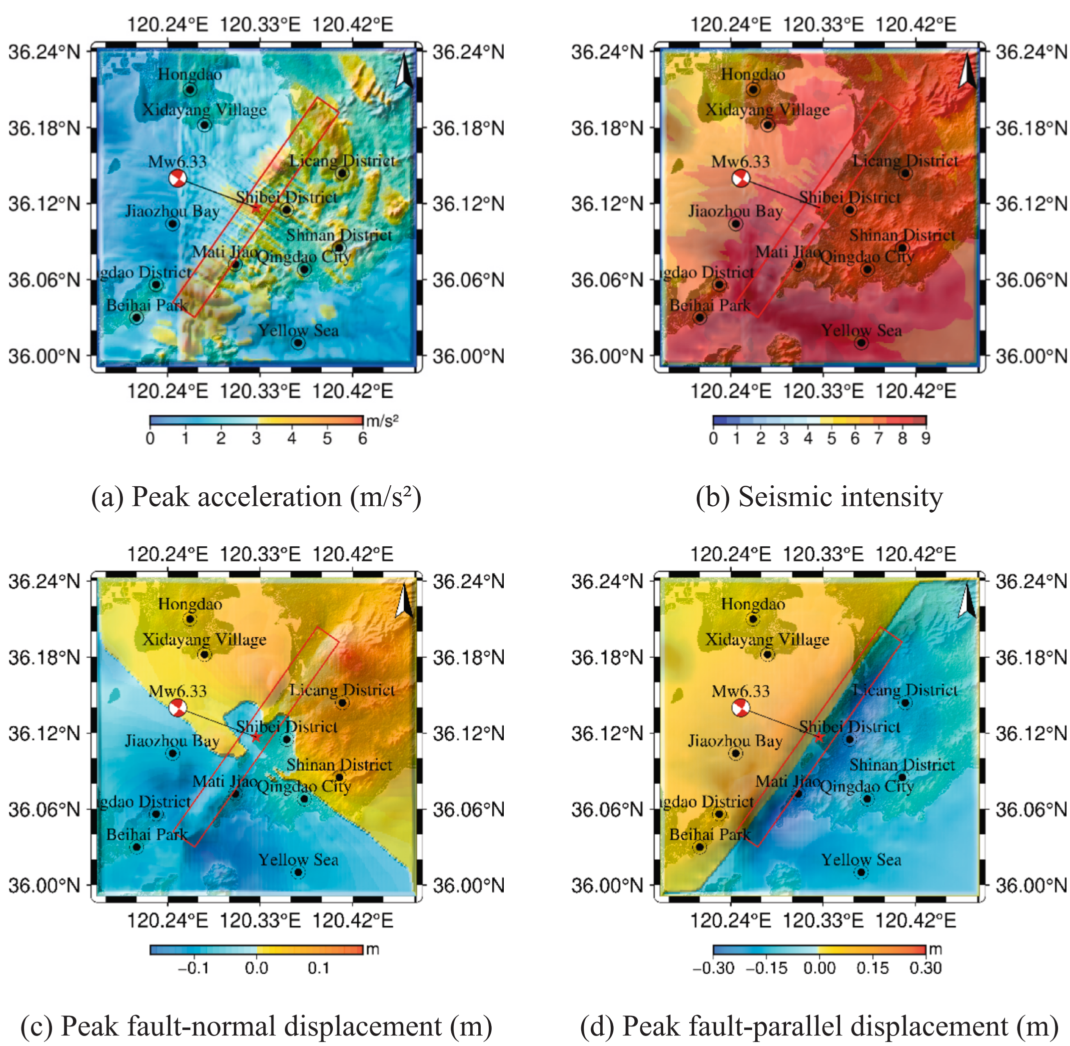

Fig. 5. Spatial distributions of simulated ground-motion parameters at the tunnel burial depth: (a) peak acceleration, (b) seismic intensity, (c) peak fault-normal displacement, and (d) peak fault-parallel displacement.

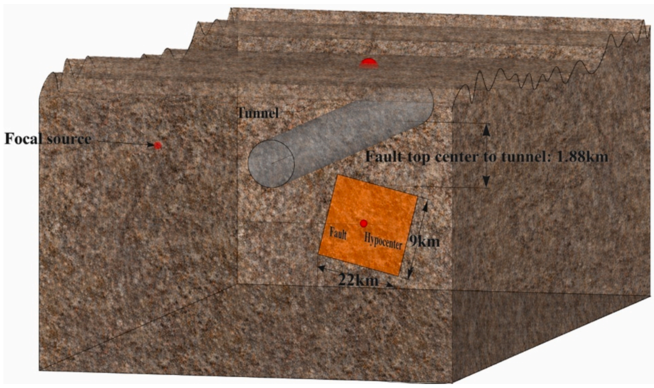

Fig. 6. Relative position between the tunnel alignment and the Cangkou Fault in the actual project.

earthquakes, including the Northridge, Kumamoto, and Menyuan earthquakes (Luo et al., 2024a). In this study, the GP rupture model was generated using the SCEC Broadband Platform (BBP) (Maechling et al., 2015), and the corresponding source parameters are listed in Table 2.

Using the source parameters listed in Table 2, the distributions of slip, rupture initiation time, and peak slip rate on the fault plane were calculated and plotted, as shown in Fig. 4.

The deepest point of the tunnel is located 120 m below sea level. Based on the ground motion simulation results, the spatial distributions of peak acceleration, seismic intensity, peak fault-normal displacement and peak fault-parallel displacement at the tunnel burial depth were obtained, as shown in Fig. 5.

As shown in Fig. 5(a), the PGA near the tunnel site ranges from approximately 0.1 g to 0.3 g, while the maximum seismic intensity at the tunnel site is about 8.5, as shown in Fig. 5(b). The peak displacement distributions in Fig. 5(c) and Fig. 5(d) indicate that the simulated displacement field exhibits clear cross-fault differences in both the fault-normal and fault-parallel directions. The largest relative displacement in the simulation domain occurs on both sides of the epicentral region, with a maximum value of approximately 46 cm. Because the tunnel site is located near the edge of the fault rupture zone, the displacement offset at the tunnel site is relatively small, with peak fault-normal and fault-parallel displacements of approximately 13 cm and 28 cm, respectively. These results suggest that the tunnel site is affected by both fault-normal and fault-parallel displacement components, which should be considered in the subsequent seismic response analysis of the tunnel.

4. Analysis cases and monitoring point arrangement

This study compares the seismic responses of six tunnel alignments within the same prescribed earthquake-source and regional-site model. Fig. 6 shows the relative position between the tunnel and the Cangkou Fault in the actual project. The seismic source is located at the geometric center of the fault plane, with a depth of 6.5 km below the ground surface, while the center of the upper edge of the fault plane is buried 2 km below the ground surface. The actual intersection angle between the surface projections of the tunnel alignment and the fault is 27°. The six alignments were generated by rotating the tunnel centerline in plan about the same fixed reference point located within the surface projection of the fault. The fault geometry and strike, hypocenter, rupture realization, regional topography and velocity structure, and the resulting regional ground-motion field were kept unchanged among the cases. The tunnel section, burial condition, material parameters, seismic-input procedure, and monitoring arrangement were also unchanged. Thus, only the alignment direction was actively changed, while the associated differences in the spatial ground-motion input sampled along each alignment arose directly from this rotation. The six cases therefore evaluate the engineering influence of changing the tunnel–fault intersection angle within the same rupture-generated regional ground-motion field. The investigated intersection angles range from 12° to 87° at an interval of 15°, as listed in Table 3.

Fig. 7 shows the relative positions between the tunnel and the fault in surface projection for Analysis Cases 1–6. To investigate the cross-fault

Table 3
Analysis cases with different tunnel-fault intersection angles.

Case	Tunnel alignment direction	Tunnel-fault intersection angle
1	47°	12°
2 (actual case)	62°	27°
3	77°	42°
4	92°	57°
5	107°	72°
6	122°	87°

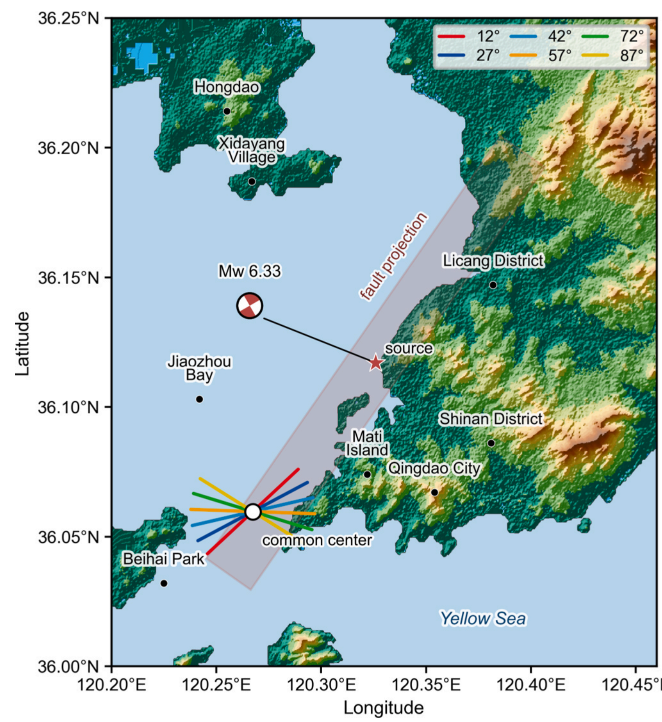

Fig. 7. Fault projection and tunnel alignments for the six intersection-angle cases. All alignments rotate about a common reference point.

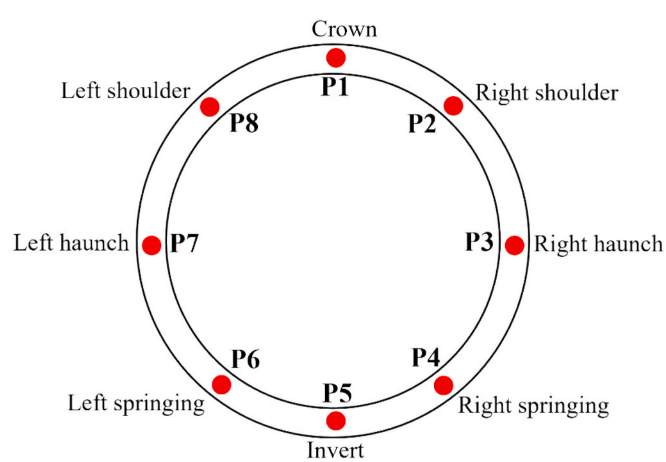

Fig. 8. Layout of monitoring points at key locations on the tunnel lining cross-section.

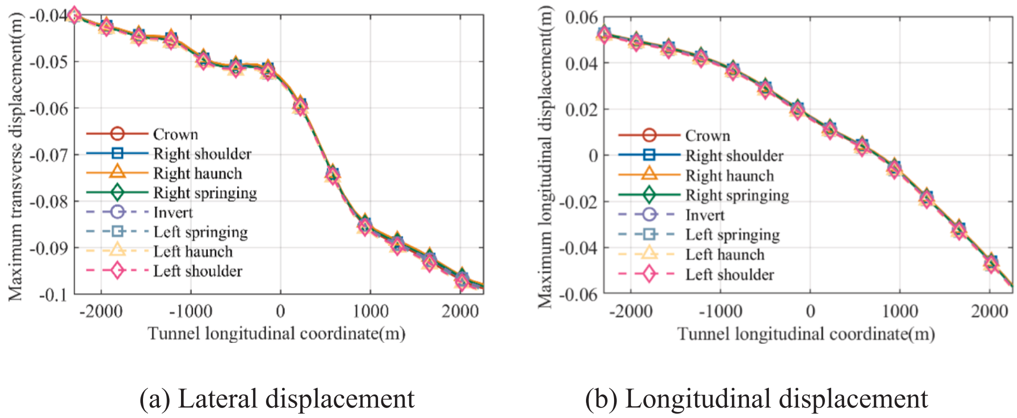

Fig. 9. Distributions of signed displacement responses at different monitoring positions of the tunnel lining at the instant of peak lateral displacement under the actual intersection angle.

seismic response of key locations of the tunnel under different cases, 39 monitoring sections were arranged along the tunnel longitudinal direction from y = -2300 m to y = 2260 m, with an interval of 120 m. Eight monitoring points were placed on each tunnel cross-section, and their layout is shown in Fig. 8.

The reported strain quantities are total mechanical strains. Radial strain and hoop strain are the normal components in the cylindrical coordinate system of the tunnel cross-section. Longitudinal normal strain and transverse normal strain are the components along the tunnel-longitudinal y direction and transverse x direction, respectively, while shear strain is the engineering shear-strain component in the global x–y plane. Equivalent strain is the von Mises-type equivalent measure calculated from the complete total mechanical strain tensor. For each alignment case, the largest equivalent strain among the 39 monitoring sections and eight circumferential positions was tracked throughout the response history. The instant at which this spatial maximum reached its overall peak was identified, and the magnitudes of all six strain quantities were extracted at that same instant. Accordingly, the strain curves report absolute magnitudes evaluated at the corresponding case-specific peak-equivalent-strain state.

5. Numerical results and discussion

5.1. Seismic response of the tunnel under the actual intersection angle

This section investigates the seismic response of the tunnel structure under the actual tunnel-fault intersection angle. The displacement and strain responses at different monitoring points are examined to clarify the deformation characteristics of the cross-fault tunnel and the corresponding response mechanisms.

5.1.1. Displacement response of the tunnel lining

Cross-fault ground motion input is characterized by pronounced spatial non-uniformity and permanent displacement. Because underground structures are constrained by the surrounding rock, their displacement responses are strongly affected by the deformation pattern of the adjacent rock mass. The displacement responses at different monitoring points were extracted after applying the cross-fault ground motion input. The lateral and longitudinal displacements of the monitoring points on each lining cross-section at the instant of peak lateral displacement were plotted against the tunnel longitudinal coordinate, as shown in Fig. 9.

Fig. 9(a) and Fig. 9(b) show the lateral and longitudinal displacement responses of the tunnel lining, respectively. The displacement responses at different monitoring points within the same lining cross-section differ only slightly; therefore, the sectional variation can be neglected when discussing the overall displacement response. When the tunnel crosses the fault at an intersection angle of 27°, the peak signed lateral displacements are all negative, indicating that the lateral displacement occurs in the same direction and does not exhibit a clear cross-fault differential pattern. However, the lateral displacement gradually increases along the tunnel longitudinal coordinate, suggesting that the tunnel lining is subjected to lateral shear deformation. In contrast, the longitudinal displacement changes gradually from negative to positive from the negative to the positive side of the tunnel axis, indicating a clear cross-fault differential deformation in the longitudinal direction. This suggests that the tunnel structure experiences axial tension–compression deformation during the seismic loading. Because the tunnel crosses above the fault and is located near the edge of the fault rupture zone, the displacement variations in both the lateral and longitudinal directions remain smooth, without abrupt changes near the cross-fault region.

5.1.2. Strain response characteristics of the tunnel lining

Based on the displacement response analysis of the monitoring points in Section 5.1.1, the strain response of the tunnel lining was further examined. As shown in Fig. 10(a–f), the distributions of radial strain, hoop strain, longitudinal normal strain, transverse normal strain, shear strain, and equivalent strain along the tunnel longitudinal direction were obtained for the lining cross-sections within the cross-fault region.

As shown in Fig. 10, the longitudinal variations of all six strain components are relatively small. This is mainly because the tunnel crosses the fault near the edge of the rupture zone, where the displacement variation of the tunnel structure is smooth and no abrupt displacement offset is induced by fault movement. This observation is consistent with the displacement offsets at the tunnel site shown in Fig. 5(c) and Fig. 5(d), as well as the displacement response of the lining shown in Fig. 9. Comparison of the six strain components in Fig. 10 indicates that the strain response of the tunnel lining is affected by both fault displacement and complex deformation of the surrounding rock. The shear strain and normal strain exhibit relatively large amplitudes, and their distribution patterns vary among different locations on the lining cross-section. For the longitudinal normal strain, the maximum value occurs at the crown, followed by the left shoulder, while the values at the other locations are relatively close. For the transverse normal strain, relatively large values are mainly observed at the right shoulder and invert, whereas the left and right haunches exhibit comparatively small strain values. The shear strain is more pronounced at the crown, right haunch, and invert, while it remains relatively small at the left and right haunches. The equivalent strain distribution in Fig. 10(f) further shows that the crown and invert are the most unfavorable locations under the actual intersection angle.

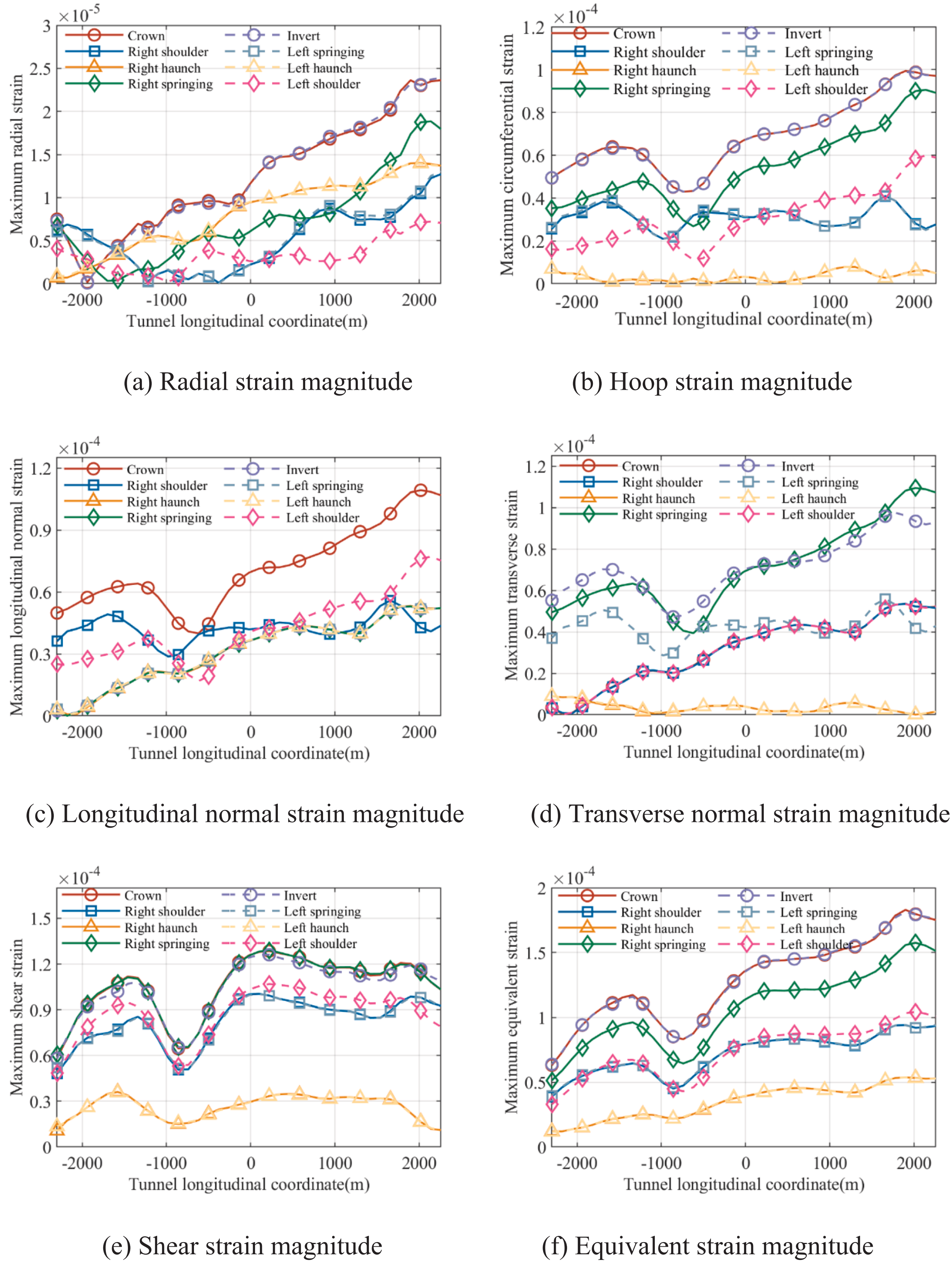

Fig. 10. Distributions of strain magnitudes at different monitoring positions of the tunnel lining, evaluated at the instant of maximum equivalent strain for the actual 27° case.

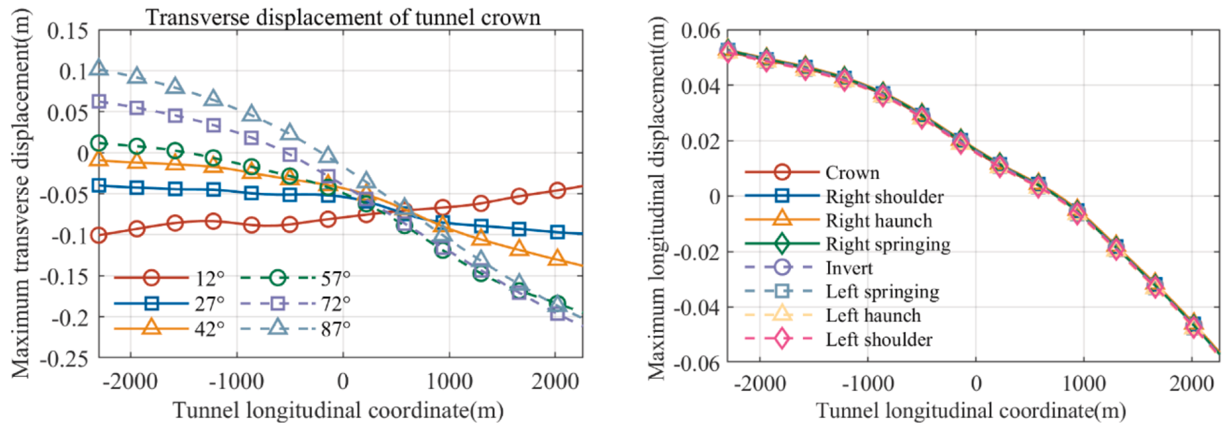

(a) Peak lateral displacement (m) (b) Peak longitudinal displacement (m)

Fig. 11. Distributions of peak displacement responses at the tunnel crown under different tunnel-fault intersection angles.

Overall, the relatively large equivalent strains at the crown and invert are associated with the combined effects of shear strain and normal strain, whereas the smaller equivalent strains at the left and right haunches result from the limited levels of both strain components. Therefore, for cross-fault tunnels without abrupt displacement offset, the potential unfavorable locations of the lining cannot be identified solely from the displacement response; instead, the combined effects of normal strain and shear strain should be considered.

5.2. Seismic response of the cross-fault tunnel under different intersection angles

5.2.1. Peak displacement response of the tunnel lining

To investigate the influence of the tunnel-fault intersection angle on the displacement response of cross-fault tunnels, the peak displacement responses at the crown monitoring point were extracted for all analysis cases within the tunnel longitudinal coordinate range from $y = -2300$ m to $y = 2260$ m. As discussed in Section 5.1.1, the displacement responses at different monitoring points on the same lining cross-section show only minor differences. Therefore, the crown displacement was selected as a representative response for comparison among different cases. The distributions of peak lateral and longitudinal displacements are shown in Fig. 11.

The displacement response changes from longitudinal-dominated to lateral-dominated deformation as the tunnel-fault intersection angle increases. For intersection angles of 12, 27, and 42 degrees, the lateral displacement varies smoothly along the tunnel axis and does not show a clear cross-fault differential pattern, whereas the longitudinal displacement exhibits a pronounced cross-fault response. At 57 degrees, both lateral and longitudinal displacements show evident differential deformation. When the angle further increases to 72 and 87 degrees, the cross-fault differential deformation is mainly reflected in the lateral displacement. Because the tunnel passes above the fault rather than directly through the fault core, the displacement field remains continuous in all cases and no abrupt local offset is observed.

This transition can be explained by the direction of rock-mass movement around the strike-slip fault. The movement on the two sides of the fault is dominated by the fault-parallel displacement component, but the fault-normal component is also non-negligible. As shown in Fig. 5(c) and Fig. 5(d), the simulated rock-mass motion contains both components, and their magnitudes are of the same order at the tunnel site. Consequently, the movement direction of the tunnel-surrounding rock is not strictly parallel to the fault strike. Even when the tunnel alignment is close to being parallel or perpendicular to the fault, the structural response cannot be simplified as pure axial deformation or pure shear deformation. The displacement response therefore identifies the dominant deformation direction, but the strain response is needed to evaluate the unfavorable combined deformation state of the lining.

5.2.2. Strain response of the tunnel lining

Based on the peak displacement responses at the tunnel crown under different analysis cases discussed in Section 5.2.1, the strain response of the tunnel lining was further analyzed. Since the equivalent strain of the lining under the actual intersection angle is relatively large at the crown and invert, as discussed in Section 5.1.2, the crown of each monitoring cross-section was selected for comparison in this section. The distributions of radial strain, hoop strain, longitudinal normal strain, transverse normal strain, shear strain, and equivalent strain at the tunnel crown within the cross-fault region are shown in Fig. 12(a–f).

The normal strain components vary markedly among the six alignment cases. The hoop and longitudinal normal strains reach their largest peak values at 42°, followed by 57° and 27°, whereas their values are smaller at 12°, 72° and 87°. The shear strain shows a different ordering, decreasing from 12°, 87°, 72°, 27° and 57° to 42°. These rankings describe the responses of the coupled alignment–input configurations within the same rupture-generated regional ground-motion field.

Direct comparison of the component peaks further illustrates these differences. At 42°, the peak hoop and longitudinal normal strains are approximately 1.22×10^{-4} and 1.26×10^{-4}, respectively, whereas the shear strain peak is approximately 0.784×10^{-4}. At 87°, the corresponding normal strain peaks decrease to approximately 0.381×10^{-4} and 0.399×10^{-4}, while the shear strain peak increases to approximately 2.03×10^{-4}. At 57°, the longitudinal normal and shear strain peaks are both appreciable, approximately 1.15×10^{-4} and 1.25×10^{-4}, and the equivalent strain reaches its largest value of approximately 2.01×10^{-4}. The similarly large shear strain peak at 12° (approximately 2.08×10^{-4}) confirms that the differences across the six cases are non-monotonic. The results therefore indicate different normal–shear strain combinations among the six alignment–input configurations, rather than a monotonic transition controlled solely by the intersection angle.

Post-processing of the plastic strain histories identified local yielding of the lining in all six discrete cases. The case-wise maximum absolute global plastic strain component ranged from 0.00210 to 0.00354, confirming an elastoplastic lining response.

Fig. 13 compares the deformed configurations and equivalent-strain distributions of the lining within the monitored cross-fault interval for all six alignment cases, each evaluated at the corresponding case-specific

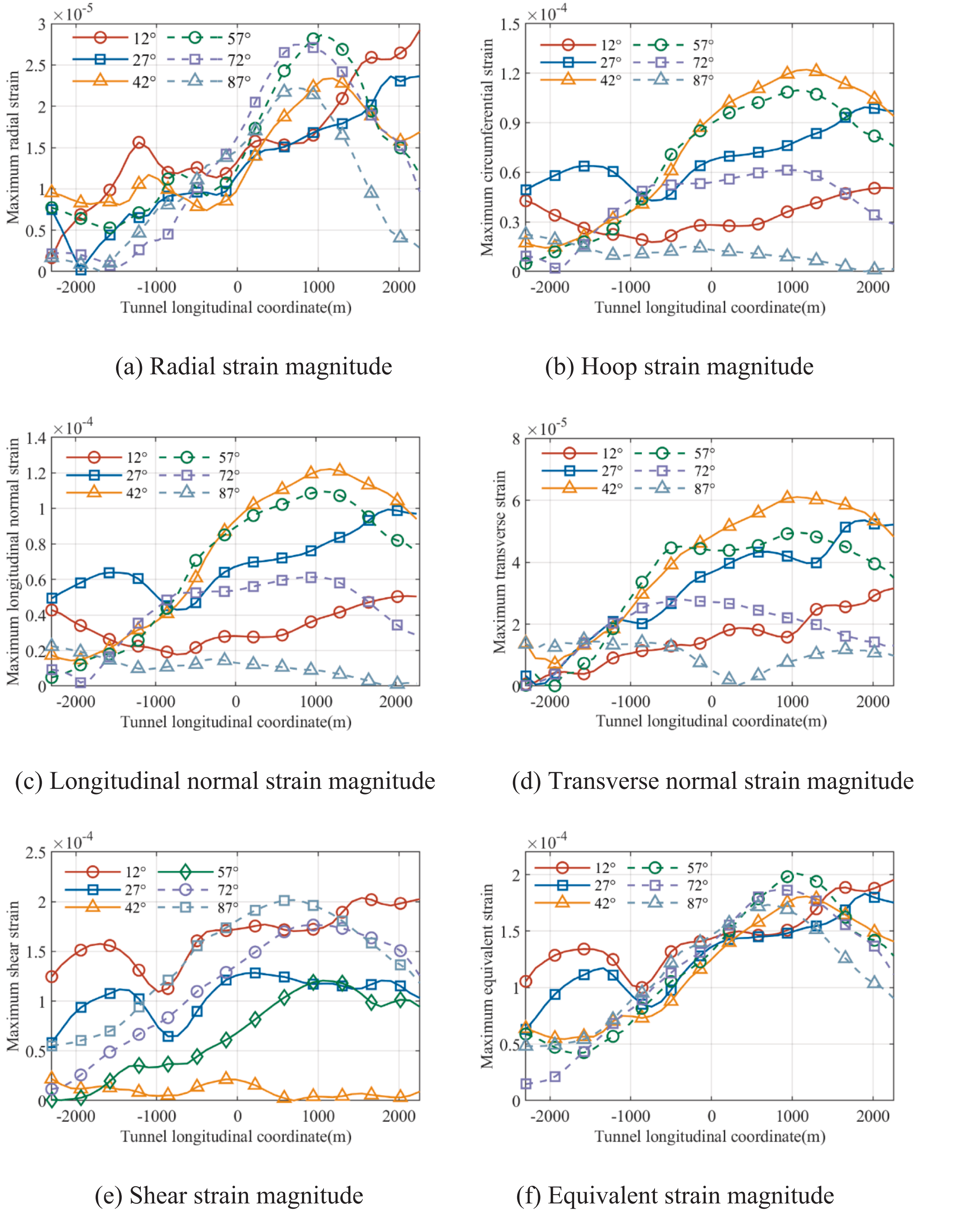

Fig. 12. Distributions of strain magnitudes at the tunnel crown for the six alignment cases, evaluated at the corresponding case-specific instant of maximum equivalent strain.

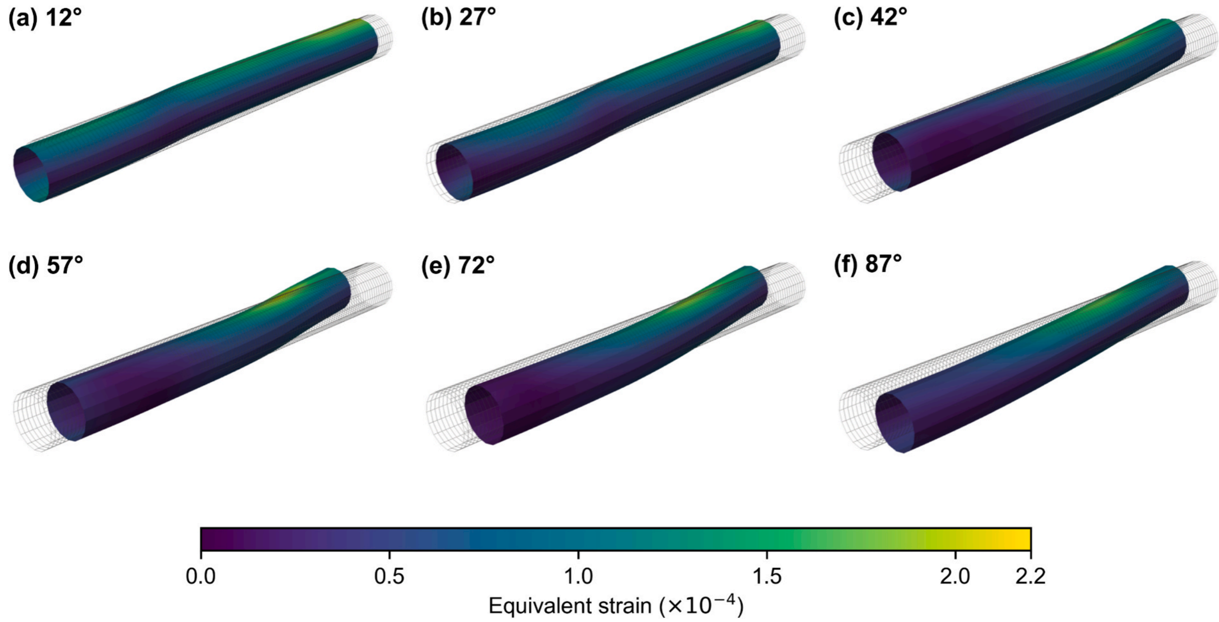

Fig. 13. Deformed configurations and equivalent-strain distributions of the tunnel lining within the monitored cross-fault interval at the corresponding case-specific reference instant defined from the peak equivalent strain at the monitoring locations: (a) 12°; (b) 27°; (c) 42°; (d) 57°; (e) 72°; and (f) 87°. The equivalent strain is evaluated from the total mechanical strain tensor, and the larger value from the inner and outer lining surfaces is shown at each node. The gray wireframe denotes the undeformed configuration. For visualization, the longitudinal dimension is shown at 3% of its geometric scale and the displacements are magnified by a factor of 80. A common strain color scale is used for all cases.

reference instant defined from the peak equivalent strain at the monitoring locations. The strain field is spatially non-uniform in all cases, while the locations and longitudinal extents of the relatively large-strain regions vary among the alignment configurations. Under the common color scale, the maximum equivalent strain ranges from approximately 1.74×10^{-4} to 2.01×10^{-4} and reaches its largest value at 57°, consistent with the longitudinal comparison in Fig. 12. The deformed configurations remain continuous in all cases, in agreement with the smooth longitudinal displacement profiles in Fig. 11. Fig. 13 therefore extends the crown-based curves in Fig. 12 to the full lining surface and shows the spatial distribution of the strain response.

These findings should be interpreted within the boundary of the present engineering case. The tunnel passes above the fault core and is located near the edge of the rupture zone; therefore, the displacement variation along the tunnel is relatively smooth and no abrupt offset is induced in the lining. Under this condition, the differences among the alignment cases are more evident in the relative prominence of the normal and shear strain components than in the peak equivalent strain. For tunnels that directly intersect the fault core, are located closer to the main rupture zone, or are subjected to larger permanent fault offsets, the same change in intersection angle may produce a more pronounced difference in equivalent strain and damage distribution.

The present comparison is based on one prescribed rupture realization and one set of fault and material parameters. The influence of alternative rupture realizations and parameter uncertainty will be investigated through multi-scenario analyses in future work.

6. Conclusions

This study investigated the seismic response of the Qingdao Jiaozhou Bay Second Subsea Tunnel crossing the Cangkou Fault by combining physics-based ground-motion simulation with MDRM-based seismic input. The actual alignment was first analyzed, followed by a comparison of six tunnel–fault alignment configurations to examine their displacement responses, strain distributions and normal–shear strain combinations. The main conclusions are as follows.

(1) For a tunnel crossing above a strike-slip fault, the rock mass motion at tunnel depth contains both fault-parallel and fault-normal displacement components. In this study, the peak fault-normal and fault-parallel displacement offsets at the tunnel site are approximately 13 cm and 28 cm, respectively. The fault-normal component is therefore smaller but still non-negligible, and the physical rupture process should be considered when defining seismic input for cross-fault tunnel response analysis.

(2) Under the actual tunnel-fault intersection angle of 27 degrees, the displacement responses at different monitoring points on the same lining section are generally consistent. Because the tunnel passes above the fault rather than directly through the fault core, the lateral and longitudinal displacement responses vary smoothly along the tunnel without abrupt offsets. The cumulative lateral displacement is approximately 6 cm, and the longitudinal compression is approximately 11 cm. The strain response shows that normal strain plays a larger role than shear strain, and the crown and invert are the most unfavorable lining locations.

(3) Under the investigated source, burial depth and tunnel configuration, the displacement response remains continuous for all six alignment cases. Among these cases, the hoop and longitudinal normal strains are relatively large and the shear strain is smallest at 42°, whereas the shear component is larger at 12°, 72° and 87°. The largest equivalent strain occurs at 57°, where both normal and shear components remain appreciable, although the difference between the maximum and minimum equivalent strains is only about 15%. The strain-component patterns vary non-monotonically across the six cases.

(4) For the present engineering condition, the differences among the six alignment cases are more pronounced in their normal–shear strain combinations than in the maximum equivalent strain alone. Seismic design and mitigation for cross-fault subsea tunnels should therefore consider the individual strain components together with the equivalent strain. These findings are specific to the prescribed earthquake-source and regional-site model and the six analyzed alignment configurations. Tunnels directly intersecting the fault core or subjected to larger permanent offsets require further assessment.

CRediT authorship contribution statement

Yang Gao: Project administration, Funding acquisition. **Ke Zhang:** Software, Formal analysis, Data curation. **Hao Wang:** Writing – review & editing, Supervision. **Zerui Ji:** Validation. **Chao Luo:** Writing – original draft, Methodology, Conceptualization.

Declaration of competing interest

The authors declare that they have no known competing financial interests or personal relationships that could have appeared to influence the work reported in this paper.

Acknowledgments

This work was supported by the National Key Research and Development Program of China [grant number 2021YFB2600800]; the National Natural Science Foundation of China [grant number 52578481]; the Scientific Research Project of Higher Education Institutions in Hebei Province [grant number CXZX2025050]; the Natural Science Foundation of Hebei Province [grant number E2024210049]; and the Earthquake Science and Technology Program of Hebei Province [grant number DZ2025092800001]. The authors thank the researchers and colleagues for valuable discussions, technical assistance, and constructive suggestions.

Data availability

Data will be made available on request.

References

Anastasopoulos, I., Gazetas, G., Bransby, M.F., Davies, M.C.R., El Nahas, A., 2008. Fault rupture propagation through sand: finite-element analysis and validation through centrifuge experiments. J. Geotech. Geoenviron. Eng. 134 (7), 943–958.

Bielak, J., Loukakis, K., Hisada, Y., Yoshimura, C., 2003. Domain reduction method for three-dimensional earthquake modeling in localized regions, Part I: Theory. Bull. Seismol. Soc. Am. 93 (2), 817–824.

China Railway Major Bridge Survey And Design Institute Group Co., Ltd. (2022). Engineering Geological Investigation Report for the Jiaozhou Bay Second Subsea Tunnel Project at the Detailed Investigation Stage. (in Chinese).

Dowding, C.H., Rozen, A., 1978. Damage to rock tunnels from earthquake shaking. J. Geotech. Eng. Div. 104 (2), 175–191.

Farr, T.G., Rosen, P.A., Caro, E., Crippen, R., Duren, R., Hensley, S., Kobrick, M., Paller, M., Rodriguez, E., Roth, L., 2007. The shuttle radar topography mission. Rev. Geophys. 45 (2).

Graves, R., Pitarka, A., 2015. Refinements to the Graves and Pitarka (2010) Broadband Ground-Motion simulation method. Seismol. Res. Lett. 86 (1), 75–80.

Graves, R., Pitarka, A., 2016. Kinematic ground-motion simulations on rough faults including effects of 3D stochastic velocity perturbations. Bull. Seismol. Soc. Am. 106 (5), 2136–2153.

Han, S., Zhang, H., Xin, H., Shen, W., Yao, H., 2022. USTClitho2.0: Updated unified seismic tomography models for continental China lithosphere from joint inversion of body-wave arrival times and surface-wave dispersion data. Seismol. Res. Lett. 93 (1), 201–215.

Hashash, Y.M.A., Hook, J.J., Schmidt, B., Yao, J.I., 2001. Seismic design and analysis of underground structures. Tunn. Undergr. Space Technol. 16 (4), 247–293.

Karamitros, D.K., Bouckovalas, G.D., Kouretzis, G.P., Gkesouli, V., 2011. A method for strength verification of buried steel pipelines at normal fault crossings. Soil Dyn. Earthq. Eng. 31 (11), 1452–1464.

Kuhlemeyer, R.L., Lysmer, J., 1973. Finite element method accuracy for wave propagation problems. J. Soil Mech. Found. Divis. 99 (5), 421–427.

Laske, G., Masters, G., Ma, Z., Pasyanos, M., 2013. Update on CRUST1.0—A 1-degree global model of Earth's crust. Geophys. Res. Abstr. 15, EGU2013-2658.

Luan, G., Wang, H., Yin, M., 2010. Characteristics of main faulted structures in Qingdao city and their influence on urban geological environment. Acta Geosci. Sin. 31 (1), 102–108 in Chinese.

Luan, G., Zhang, H., 2001. Plane geometry and modern activity of the Qingdao Cangkou-Wenquan fault. Seismol. Geol. 23 (1), 61–68 in Chinese.

Luo, C., Cao, X., Gao, Y., Xu, F., Feng, H., Wang, H., 2024a. Applicability study of the GP fault rupture model in strong ground motion simulation for the Qinghai Menyuan Ms6.9 earthquake. Chin. J. Geophys. 67 (2), 534–547 in Chinese.

Luo, C., Cao, X., Gao, Y., Xu, F., Xu, Y., Wang, H., 2024b. Physics-based seismic response analysis method for tunnels crossing faults. J. Vibrat. Shock 43 (22), 293–304 in Chinese.

Luo, C., Du, H., Du, Y., Bu, X., Xu, F., Zheng, H., Wang, H., Ji, Z., 2026. Evaluation of ground-motion intensity measures for seismic response of fault-crossing tunnels. Tunn. Undergr. Space Technol. 176, 107885. https://doi.org/10.1016/j.tust.2026.107885.

Luo, C., Lou, M., Gui, G., Wang, H., 2019. A modified domain reduction method for numerical simulation of wave propagation in localized regions. Earthq. Eng. Eng. Vib. 18 (1), 35–52.

Luo, X., Wang, M., Yu, L., 2023. Computational model of three-dimensional mechanical response of tunnel under uneven slip of oblique-slip fault. Modern Tunnelling Technol. 60 (4), 86–94,146.

Lysmer, J., Kuhlemeyer, R.L., 1969. Finite dynamic model for infinite media. J .Eng. Mech. Div. 95 (4), 859–877.

Maechling, P.J., Silva, F., Callaghan, S., Jordan, T.H., 2015. SCEC broadband platform: system architecture and software implementation. Seismol. Res. Lett. 86 (1), 27–38.

Petersson, N. A., & Sjögreen, B., 2017. User's guide to SW4, version 2.0. *Lawrence Livermore National Laboratory Tech. Rept.* LLNL-SM-741439.

Qiao, Y., Tang, J., Liu, G., He, M., 2022. Longitudinal mechanical response of tunnels under active normal faulting. Underground Space 7 (4), 662–679.

Sharma, S., Judd, W.R., 1991. Underground opening damage from earthquakes. Eng. Geol. 30 (3–4), 263–276.

Tsinidis, G., de Silva, F., Anastasopoulos, I., Bilotta, E., 2020. Seismic behaviour of tunnels: from experiments to analysis. Tunn. Undergr. Space Technol. 99, 103334.

Vazouras, P., Karamanos, S.A., Dakoulas, P., 2012. Mechanical behavior of buried steel pipes crossing active strike-slip faults. Soil Dyn. Earthq. Eng. 41, 164–180.

Wang, H., Luo, C., Wan, J., Zhu, M., Lou, M., Feng, H., 2021. A hybrid boundary method for seismic wave propagation problems in slopes. Soil Dyn. Earthq. Eng. 147, 106773.

Wang, J. (2021). Seismic Safety Evaluation Report for the Jiaozhou Bay Second Subsea Tunnel Project Site: National Institute of Natural Disaster Prevention and Control, Ministry of Emergency Management. (in Chinese).

Wells, D.L., Coppersmith, K.J., 1994. New empirical relationships among magnitude, rupture length, rupture width, rupture area, and surface displacement. Bull. Seismol. Soc. Am. 84 (4), 974–1002.

Xia, C., Wang, Z., He, Y., Chen, Y., Li, C., Shi, L., Zhao, C., 2024. Seismic response of mountain tunnel induced by fault slip. Sci. Rep. 14 (1), 17768.

Yoshimura, C., Bielak, J., Hisada, Y., Fernandez, A., 2003. Domain reduction method for three-dimensional earthquake modeling in localized regions, Part II: verification and applications. Bull. Seismol. Soc. Am. 93 (2), 825–841.

Zhang, R. (2012). Seismic response analysis of large underground structure–soil dynamic interaction system [Doctoral dissertation, Tongji University]. Shanghai, China.

Zhao, D., Wang, Y., Ren, Z., 2023. Mechanical response analysis of tunnel structure considering the combined effect of fault dislocation and ground motion. Modern Tunnell. Technol. 60 (4), 95–105 in Chinese.

Zhu, H., Yu, H., Han, F., Wei, Y., Yuan, Y., 2023. Seismic resilience design principles and key issues for tunnels crossing active faults. China J. Highway and Transport 36 (11), 193–204. https://doi.org/10.19721/j.cnki.1001-7372.2023.11.002 (in Chinese).